NREL
NATIONAL RENEWABLE ENERGY LABORATORY

A Large-Eddy Simulation Study of Wake Propagation and Power Production in an Array of Tidal-Current Turbines

Preprint

M.J. Churchfield, Y. Li, and P.J. Moriarty

To be presented at the 9th European Wave and Tidal Energy Conference 2011
Southhampton, England
September 4 – 9, 2011

Conference Paper
NREL/CP-5000-51765
July 2011

Contract No. DE-AC36-08GO28308

NOTICE

Available electronically at http://www.osti.gov/bridge

Available for a processing fee to U.S. Department of Energy
and its contractors, in paper, from:

U.S. Department of Energy
Office of Scientific and Technical Information

P.O. Box 62
Oak Ridge, TN 37831-0062
phone: 865.576.8401
fax: 865.576.5728
email: mailto:reports@adonis.osti.gov

Available for sale to the public, in paper, from:

U.S. Department of Commerce
National Technical Information Service
5285 Port Royal Road
Springfield, VA 22161
phone: 800.553.6847
fax: 703.605.6900
email: orders@ntis.fedworld.gov
online ordering: http://www.ntis.gov/help/ordermethods.aspx

Cover Photos: (left to right) PIX 16416, PIX 17423, PIX 16560, PIX 17613, PIX 17436, PIX 17721

Printed on paper containing at least 50% wastepaper, including 10% post consumer waste.

A Large-Eddy Simulation Study of Wake Propagation and Power Production in an Array of Tidal-Current Turbines

Matthew J. Churchfield[1], Ye Li[2], Patrick J. Moriarty[3]

National Wind Technology Center, National Renewable Energy Laboratory
1617 Cole Boulevard, Golden, CO 80401 USA

[1]Matt.Churchfield@nrel.gov

[2]Ye.Li@nrel.gov

[3]Patrick.Moriarty@nrel.gov

***Abstract*— This paper presents our initial work in performing large-eddy simulations of tidal turbine array flows. First, a horizontally-periodic precursor simulation is performed to create turbulent flow data. Then that data is used as inflow into a tidal turbine array two rows deep and infinitely wide. The turbines are modelled using rotating actuator lines, and the finite-volume method is used to solve the governing equations. In studying the wakes created by the turbines, we observed that the vertical shear of the inflow combined with wake rotation causes lateral wake asymmetry. Also, various turbine configurations are simulated, and the total power production relative to isolated turbines is examined. Staggering consecutive rows of turbines in the simulated configurations allows the greatest efficiency using the least downstream row spacing. Counter-rotating consecutive downstream turbines in a non-staggered array shows a small benefit. This work has identified areas for improvement, such as the use of a larger precursor domain to better capture elongated turbulent structures, the inclusion of salinity and temperature equations to account for density stratification and its effect on turbulence, improved wall shear stress modelling, and the examination of more array configurations.**

***Keywords*— tidal, turbine, array, LES, CFD**

I. INTRODUCTION

Interest is growing in the large-scale deployment of marine hydrokinetic (MHK) energy capture devices. One such device is the horizontal-axis tidal turbine (HATT). Currently, companies such as Verdant Power and Marine Current Turbines are well on their way to developing commercially-viable HATTs. For example, Verdant has deployed six turbines with rotors of 5m in diameter in an array in the East River in New York City (RITE project), and MCT has deployed a 1.2MW dual-rotor system in Strangford Lough in Northern Ireland (SeaGen project).

To make efficient use of tidal regions, HATTs will be arranged in arrays of multiple turbines. These devices are much like horizontal-axis wind turbines, creating wakes as a by-product of energy extraction. If a downstream turbine is within the wake of an upstream turbine, there is less energy to extract from the flow and there can be increased turbulence.

There is a limited understanding of how these wakes affect the performance and mechanical loading of downstream turbines. It also is unclear how wakes interact with the turbulence in the ambient tidal flow. Among other things, turbulence in the tidal flow is affected by the roughness of the lower surface of the tidal channel and density gradients in the flow due to temperature and salinity stratification, which change throughout a tidal cycle. An array of HATTs can be designed to take advantage of the bi-directionality of the ebb and flow of tidal regions. There is a predominant streamwise flow direction, so the turbines can be closely spaced in the cross-stream direction since the low-energy wakes are unlikely to propagate in that direction.

A necessary step in better understanding the flow physics is to take wake and inflow measurements in an array of HATTs; however, it is a costly endeavour. A complement to such measurements is computational fluid dynamics (CFD). CFD can give insight into the physics of the flow and highlight phenomena that should be verified by experimental measurement. CFD also gives a complete picture of the flow field. Using a combination of CFD and experimental measurements will lead to an increased understanding of tidal turbine array and tidal channel physics. This knowledge is necessary to create lower-order engineering tools that developers can use to plan efficient tidal turbine arrays.

The focus of this paper is to present our initial work, using CFD, to simulate tidal turbine array flows, specifically arrays of HATTs. Our current simulations are not meant to capture all of the physics of tidal flows—this is a work in progress. The effects of density stratification, tidal channel topography, tidal-cycle flow variation, or free-surface effects are not included. We have simplified the tidal channel flow by making it periodic in the cross-stream direction during the turbine array simulations and periodic in both horizontal directions during the precursor turbulence spin-up. Furthermore, the flow is approximated to have constant density and is driven by a body force to a time-invariant turbine hub height average speed. Rotating actuator lines impose forces on the flow to mimic the effect of the turbines. The type of CFD employed is large-eddy simulation (LES), in which the larger turbulent scales are resolved rather than modelled. This work is meant to develop a framework for generating inflow tidal channel turbulence, feeding that into a

tidal turbine array, and modelling the effects of the turbines on the flow and on each other. Further detail will be incrementally added in the future. In setting up this framework, we studied the effect of array layout on overall power production and the characteristics of the turbine wakes.

To our knowledge, there are no other published works in which LES is used to simulate tidal turbines. However, a number of researchers have used CFD, based on the Reynolds-averaged Navier-Stokes (RANS) equations, for this purpose. Others have used LES to simulate the tidal flow without turbines. We also are not aware of any tidal turbine work in which an actuator line model for the turbines has been used, although that model is used for wind turbine work.

MacLeod et al. [1] use RANS-based CFD, in which the turbine is modelled as a disk through which there is a pressure jump. That group focused on the wakes generated by one turbine or tandem turbines. They explored the effect of ambient turbulence on wake recovery and found that, as expected, the wake recovers more rapidly with downstream distance as the ambient turbulence level is increased.

Gant and Stallard [2] used steady and unsteady RANS-based CFD to study a single turbine in a tidal channel flow. Like [1], their turbine is modelled as a disk through which pressure decreases. This study attempted to provide unsteady turbulent inflow, generated by imposing fluctuations onto a power-law mean velocity profile. The fluctuations were derived from either a von Kármán spectral approach or a "Synthetic Eddy Method." They found that the unsteady flow imposed at the upstream boundary decays with downstream distance, as is to be expected with RANS. Nonetheless, they found that wake recovery with downstream distance was enhanced by using the unsteady inflow. This highlights the point that proper inflow modelling and characterization is important in accurately simulating tidal turbine arrays.

Sun et al. [3] used RANS-based CFD to examine the flow past a small turbine in a small channel. They modelled the turbine as a porous disk and the upper surface of the channel as a free surface using the volume-of-fluid method. They performed both two- and three-dimensional calculations to show that the turbine has a considerable effect on the free-surface elevation, which, in turn, causes a local acceleration of fluid above the turbine. This free-surface disturbance, they argue, has a significant effect on the way in which the turbine wake develops with downstream distance.

With the exception of [2], these previous studies focus more on the effects of placing turbines in the flow than on the turbulent inflow. Li et al. [4] examined the inflow by performing LES to simulate the tidal-cycle variation of tidal flow, without the influence of turbines. This work includes the effects of salinity and temperature stratification and a cyclically-varying force that drives the flow. It shows how the mean velocity, salinity, and the nature of the turbulence vary during a tidal cycle. These effects are important in understanding the performance of tidal turbine arrays and how turbine wakes develop. These effects will be included in our future simulations. Lower-order tools used to plan tidal turbine arrays should incorporate such effects.

The effects of tidal channel topography could be important in simulating tidal turbine arrays, but we are unaware of research that explores this in the context of array simulations. Researchers are, however, using various types of CFD to study how channel topography, in the absence of turbines, affects the flow. Examples include the work of Zhao [5], in which LES was used to compute the flow through a tidal channel on the central California coast, and that of Booij [6], in which RANS and LES are compared when computing flow in curved tidal channels and rivers.

II. Large-Eddy Simulation Methodology

LES is the CFD method used in this study. The larger turbulent scales are directly resolved by solving the spatially-filtered Navier-Stokes equations, whereas the effects of the remaining, more isotropic, smaller scales are modelled with a sub-filter-scale (SFS) turbulence model. LES provides more flow-physics detail, and it places less reliance on turbulence modelling than the more computationally-efficient Reynolds-averaged Navier-Stokes (RANS) type of CFD, in which all turbulent scales are modelled. Unlike direct numerical simulation (DNS), in which all turbulent scales are resolved, LES remains computationally-tractable at the high Reynolds number of this flow. The larger scales are not resolved near the lower tidal surface; instead, we use a wall model.

The turbine geometry is not resolved (i.e., a grid is not fitted around the blades and the support structure). Rather, we use actuator lines in which the forces created by the turbine are modelled and applied to the flow field as a body force.

The simulations are performed in two stages. In the first stage, the precursor simulation, the turbulence is allowed to develop without the influence of the turbines. The tidal flow is approximated as infinite in both of the horizontal directions through the use of periodic boundary conditions. As the simulation progresses in time, the turbulence reaches a quasi-steady state. Then, data are taken from a streamwise boundary plane and saved at each time step over some time interval. They are used as the inflow boundary condition for the second stage of the simulations, in which a turbine array is introduced. Streamwise periodicity is no longer assumed. Turbulent inflow generated during the precursor stage enters the domain, is perturbed by the turbines, and then the flow containing the turbine wakes is allowed to exit the domain and does not cycle back through.

A. Resolved-Scale Governing Equations

With LES, the incompressible Navier-Stokes equations are spatially-filtered to arrive at the resolved-scale (large-eddy scale) equations of motion. The filtered continuity equation is

$$\frac{\partial \overline{u}_j}{\partial x_j} = 0 \,, \tag{1}$$

where the overbar denotes filtering and $\overline{u}_j = u_j - u'_j$ is the resolved-scale velocity vector, which is the instantaneous velocity vector, u_j, minus the SFS velocity vector, u'_j. (Please note that a finite-volume formulation is used and a

filter is not explicitly applied, as is often done with pseudo-spectral calculations. Rather, the finite-volume formulation itself acts as a box filter.) The filtered momentum equation is

$$\frac{\partial \overline{u}_i}{\partial t} + \frac{\partial}{\partial x_j}\left(\overline{u}_j \overline{u}_i\right) = -\frac{\partial \widetilde{p}}{\partial x_i} - \frac{\partial \tau_{ij}^D}{\partial x_j} + F_i^T + F_i^A, \tag{2}$$

where $\widetilde{p} = (\overline{p} + \tau_{kk}/3)/\rho$ is a modified pressure consisting of the resolved pressure, $\overline{p}$, normalized by the constant density, ρ, plus a contribution from the normal SFS stresses, τ_{kk}. The tensor $\tau_{ij}^D = \tau_{ij} - \tau_{kk}\delta_{ij}/3$ is the deviatoric part of the full density-normalized SFS stress tensor, τ_{ij}, which arises due to spatially filtering the non-linear convective term. F_i^T and F_i^A are the density-normalized forces that drive the tidal flow and due to the actuator line representation of the turbine, respectively. In reality, F_i^T, is a cyclically-varying force that causes tides to ebb and flow. In our simulations, F_i^T adjusts with time to drive the flow to a time-invariant value of 1.9m/s at the turbine hub height. Because this is a high Reynolds number flow, the viscous stresses only become significant near the wall. However, we use a wall model that includes the total viscous and SFS stresses in that region. Therefore, Equation 2 does not explicitly include a viscous term. It is important to note that we neglected the effects of buoyancy, which can act to suppress or enhance turbulence production, and Coriolis forces due to the Earth's rotation. Buoyancy effects arise due to density variations caused by both temperature and salinity stratification.

B. Sub-Filter-Scale Model

The deviatoric part of the SFS stress, the quantity upon which the divergence operator is acting in the second term of the right-hand side of Equation 2, is defined as

$$\tau_{ij}^D = -2\nu^{SFS}\overline{S}_{ij}, \tag{3}$$

where ν^{SFS} is the SFS viscosity, and

$$\overline{S}_{ij} = \frac{1}{2}\left(\frac{\partial \overline{u}_i}{\partial x_j} + \frac{\partial \overline{u}_j}{\partial x_i}\right) \tag{4}$$

is the resolved strain-rate tensor. The SFS viscosity in Equation 3 is found using the Smagorinsky model [7]

$$\nu^{SFS} = (C_s\Delta)^2(2\overline{S}_{ij}\overline{S}_{ij})^{1/2}, \tag{5}$$

where C_s is the model constant set to 0.125, and Δ is the filter length scale, which is defined as $\Delta = (\Delta x \Delta y \Delta z)^{1/3}$, where Δx, Δy, and Δz are the grid spacing in the streamwise, cross-stream, and vertical directions, respectively.

C. Boundary/Initial Conditions and Computational Domain

In this study, we approximate a tidal flow through a wide channel. For example, channels within Washington's Puget Sound have been identified as excellent sites for deployment of MHK energy devices [8]. Some of those channels are a few kilometers wide and tens of meters deep.

Since we are simulating a large channel, in the precursor stage of the simulation when inflow turbulence is developed without the influence of the turbines, the flow is assumed to be horizontally-infinite and of uniform depth through the use of periodic boundary conditions on velocity, pressure, and SFS stresses in the streamwise and cross-stream directions. The simulation is initialized with divergence-free organized perturbations near the lower surface superimposed upon a logarithmic mean velocity profile.

In the second stage of the simulation, we simulate the tidal turbine array. Periodic boundary conditions on velocity, pressure, and SFS stresses are applied in the cross-stream direction. Space- and time-varying velocity data saved from the precursor simulation are used as an upstream boundary condition. On the downstream boundary, the normal velocity gradient of velocity is zero, and the resulting velocity flux through that boundary is adjusted to maintain global continuity. SFS stresses on the upstream and downstream boundaries are based on velocity gradients computed using one-sided differences. The gradient of pressure normal to the upstream and downstream boundaries is zero. The array simulations are initialized with the precursor flow field saved when we began to collect precursor boundary data.

The upper boundary remains the same during the precursor and array simulations. It is approximated as an impenetrable, no stress lid, instead of simulating a free surface. The velocity normal to the boundary, the gradient of velocity parallel to the boundary, all components of the SFS stress tensor, and the gradient of pressure normal to the boundary are all zero.

The lower boundary remains the same during the precursor and array simulations, as well. The normal gradient of pressure is zero. Since we are modelling the lower boundary as a rough surface, the velocity normal to the surface is zero, and there is no need to specify the horizontal velocity. The no-slip condition is not appropriate on a rough surface in which the roughness elements are not resolved since the mean velocity goes to zero at the aerodynamic roughness height, z_0. Instead, the total of the viscous and SFS stresses on the lower boundary are modelled and applied following the work of Moeng [9]. On this boundary, the total stress tensor is

$$\tau_{ij}^D = \begin{pmatrix} 0 & 0 & \tau_{xz}^D \\ 0 & 0 & \tau_{xz}^D \\ \tau_{xz}^D & \tau_{yz}^D & 0 \end{pmatrix}. \tag{6}$$

Only two components are unique, and they are modelled as

$$\tau_{xz}^D = -u_*^2 \frac{S_{1/2}\langle \overline{u}_{1/2}\rangle + \langle S_{1/2}\rangle\left(\overline{u}_{1/2} - \langle \overline{u}_{1/2}\rangle\right)}{\langle S_{1/2}\rangle\left(\langle \overline{u}_{1/2}\rangle^2 + \langle \overline{v}_{1/2}\rangle^2\right)^{1/2}} \tag{7}$$

and

$$\tau_{yz}^D = -u_*^2 \frac{S_{1/2}\langle \overline{v}_{1/2}\rangle + \langle S_{1/2}\rangle\left(\overline{v}_{1/2} - \langle \overline{v}_{1/2}\rangle\right)}{\langle S_{1/2}\rangle\left(\langle \overline{u}_{1/2}\rangle^2 + \langle \overline{v}_{1/2}\rangle^2\right)^{1/2}}, \tag{8}$$

where the subscript "1/2" refers to values at the centers of the cells adjacent to the surface (values at one-half the grid cell height), angle brackets denote horizontal averaging, $S = (\overline{u}^2 + \overline{v}^2)^{1/2}$ is the magnitude of the resolved horizontal velocity, and $\overline{u}$ and $\overline{v}$ are the *x*- and *y*-directed resolved velocity components, respectively. u_* is the friction velocity, which is related to the mean surface stress as

$$u_* = \left[\left\langle \tau_{xz}^D \right\rangle^2 + \left\langle \tau_{yz}^D \right\rangle^2 \right]^{1/4}. \quad (9)$$

To solve Equations 7 and 8, u_* is needed. Assuming that the first grid level cell centers lie within the surface layer of the tidal boundary layer, friction velocity is estimated using the log law for rough walls

$$\frac{\langle U_{1/2} \rangle}{u_*} = \frac{\left(\langle \overline{u}_{1/2} \rangle^2 + \langle \overline{v}_{1/2} \rangle^2 \right)^{1/2}}{u_*} = \frac{1}{\kappa} \ln\left(\frac{z_{1/2}}{z_0} \right), \quad (9)$$

where $z_{1/2}$ is one-half the height of the grid cells adjacent to the lower surface, z_0 is the aerodynamic roughness height, and κ is the von Kármán constant. In this study, we have taken z_0 as 4cm and κ as 0.41.

The domain measures 240m × 80m × 70m in the streamwise, cross-stream, and vertical directions, respectively. There are 410 × 180 × 160 grid cells in each of these directions yielding a grid resolution of roughly 0.5m in all directions. The domain is longer in the streamwise direction than the cross-stream in an attempt to capture the elongated streamwise turbulent structures in the boundary layer, and to allow for a small array of turbines that would be less closely spaced in the streamwise direction than in the cross-stream.

D. Turbine Model

The geometry of the turbine is not resolved because that would require such small grid spacing near the surface of the structure as to render the computation infeasible. The wall model that we use to avoid that issue for the lower surface of channel is not designed to model the turbulence near the turbine structure surfaces. Instead, the turbine is represented using Sørensen and Shen's actuator line model [10] that imposes body forces on the flow equal and opposite to the lift and drag forces experienced by the turbine.

Each turbine blade is represented as an actuator line. Each actuator line is divided into a number of equally-spaced segments. In this study, there are forty segments per line. The blade airfoil type, chord, twist, and local flow velocity are known at the center-point of each actuator segment. With that information and the rotor speed, the velocity magnitude, V_{mag}, and local flow angle, α_{local}, can be computed. The local flow angle is different than the angle-of-attack, α. The angle-of-attack is the angle between the airfoil chord line and the freestream, whereas the local flow angle is the angle between the airfoil chord line and the local flow. When an airfoil creates lift, there is an upwash in front of the airfoil due to the bound circulation, which causes the flow to curve upward. This means that $\alpha < \alpha_{local}$. We currently do not include a correction for this, and we assume $\alpha = \alpha_{local}$. In the future, we will incorporate a correction like that discussed in [11]. Employing lift and drag look-up tables for the rotor airfoils, the magnitude of lift, *L*, and drag, *D*, normalized by density at each actuator segment can be computed using

$$L = \frac{1}{2} C_l(\alpha) V_{mag}^2 cw \quad (10)$$

and

$$D = \frac{1}{2} C_d(\alpha) V_{mag}^2 cw, \quad (11)$$

where C_l and C_d are the lift and drag coefficients, respectively, *c* is the chord length, and *w* is the actuator segment width. Knowing that lift and drag forces act perpendicular and parallel to the oncoming wind vector, respectively, one uses those forces to form the total force vector experienced by the turbine, $f_i^{turbine}$.

Each actuator segment has its own value of $f_i^{turbine}$, which is a point force that cannot be directly applied to the flow field, rather it must be projected onto the flow field volume. The volume integral of the volume-projected force must be the same as the original actuator segment force. Following [10], the projected force at a grid cell located at (x, y, z) is related to the actuator segment forces using a Gaussian projection as follows:

$$F_i^A(x,y,z,t) = -\sum_{j=1}^{N} f_i^{turbine}(x_j, y_j, z_j, t) \frac{1}{\varepsilon^3 \pi^{3/2}} \exp\left[-\left(\frac{|\vec{r}|}{\varepsilon} \right)^2 \right]. \quad (12)$$

The summation is calculated over all *N* actuator segments of the turbine. The location of the j^{th} segment is (x_j, y_j, z_j), where $|\vec{r}|$ is the magnitude of the vector between (x, y, z) and (x_j, y_j, z_j), ε controls the width of Gaussian, and the negative sign accounts for the fact that the force that the turbine exerts on the flow field is equal and opposite to the force it experiences due to the flow. ε is equal to twice the cube root of the volume of the cells local to the turbine. (The cells local to the turbine all have the same volume so ε is a constant.) This value of ε is roughly the minimum value at which the force is smoothed enough to avoid spurious oscillations in the resulting velocity field.

The turbine being modelled is a hypothetical 550 kW two-bladed machine meant to operate in flow speeds ranging from 0.5 to 3.0 m/s. It has a 20m rotor diameter with NACA 63 series sections. This design has been extensively analyzed by researchers at the National Renewable Energy Laboratory (NREL), and is outlined in [12].

E. Numerical Method

Our solver was created using the OpenFOAM (*Open F*ield *O*perations and *M*anipulations) CFD toolbox [13]. The

OpenFOAM software is a set of C++ libraries meant for solving partial differential equations. The governing equations are solved using the finite-volume method. Although the solver is unstructured, our grid is composed of hexahedral elements and could be described in a structured way. All variables, except SFS viscosity and stress, are cell-centered and collocated on the grid. SFS viscosity and stress are located on cell faces. To avoid the pressure-velocity decoupling that occurs with collocated, incompressible solvers, the velocity fluxes at the finite-volume faces are constructed using an interpolation similar to that in Rhie and Chow [16]. All other interpolations from cell centers to faces are linear, which is similar to second-order central finite differencing. Time advancement uses the PISO (*P*ressure-*I*mplicit *S*plitting *O*peration) algorithm [17], which is a semi-implicit predictor-corrector scheme. We say it is "semi-implicit" because we do not treat all the terms implicitly. The SFS stresses, turbine forces, and velocity flux within the convective term of the momentum equation are treated explicitly to avoid iterating during each time-step. The implicit terms are integrated in time using Crank-Nicholson discretization. One predictor followed by three correctors are used. The momentum equation (Equation 2) is solved directly. However, to enforce the continuity equation (Equation 1), the divergence of the discrete momentum equation is used, which results in an elliptic equation for pressure. It is solved using an iterative diagonal incomplete-Cholesky pre-conditioned conjugate-gradient linear system solver. The momentum equation is solved using an iterative diagonal incomplete-LU pre-conditioned biconjugate-gradient linear system solver. The code is parallelized using the message-passing interface (MPI).

III. Cases Simulated

A. *Precursor Simulation*

The precursor simulation is run for 6000s, which corresponds to seven large-eddy turnover times, where a large-eddy turnover time is defined as $\tau_* = d/u_*$ and d is the channel depth of 70m. Although [18] states that six large-eddy turnover times are sufficient to reach a quasi-steady state in planetary boundary layer flows, we need to perform a more definitive study to determine the time at which the quasi-steady state occurs for this type of flow. Beginning at 6000s, planes of velocity boundary data in the streamwise direction are collected for an additional 500s to be used as inflow for the turbine array simulations. The volume flow field at 6000s is used as the initial flow field for the array simulations.

B. *Tidal Turbine Array Simulations*

Ten different turbine array cases are computed using the same inflow and initialization data from the precursor simulation in all cases. Fig. 1 shows the plan view of the turbine array, in a non-staggered or staggered configuration. The downstream spacing, S_1, and the cross-stream spacing between rotor disks, S_2, is variable. The turbines are labelled T0, T1, T2, T3, and T4. Outlined in Table I, each case has different streamwise and cross-stream turbine spacings, a different turbine rotor rotation sense, and consecutive rows have stagger or no stagger.

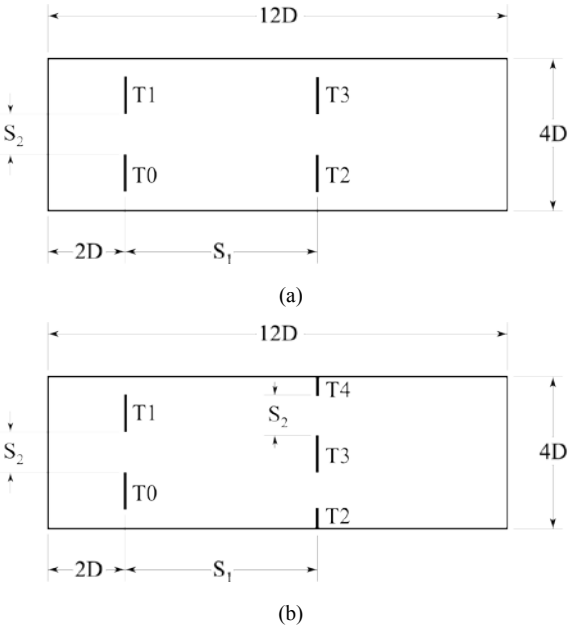

Fig. 1 Plan view of tidal turbine array in (a) non-staggered and (b) staggered configuration. Flow is from left to right.

TABLE I
Summary of Different Turbine Array Cases

	Spacings		Rotor Rotation Direction				
Case	**S_1**	**S_2**	**T0**	**T1**	**T2**	**T3**	**T4**
A	–	–	cw	–	–	–	–
B	4D	1D	cw	cw	cw	cw	–
C	5D	1D	cw	cw	cw	cw	–
D	6D	1D	cw	cw	cw	cw	–
E	4D	1D	ccw	cw	ccw	cw	–
F	4D	1D	ccw	cw	cw	ccw	–
G	4D	1/2D	ccw	cw	ccw	cw	–
H	4D	1/8D	ccw	cw	ccw	cw	–
I	4D	1D	cw	cw	cw	cw	cw
J	4D	1D	ccw	cw	cw	ccw	cw

IV. Results

A. *Precursor Simulation*

During the precursor simulation, statistics are gathered during between 5500 and 6500s. Fig. 2 shows the mean horizontal velocity profile of the precursor tidal channel flow. The turbine rotor disk lies between the dotted lines. It shows that the mean velocity at hub height (z/d = 0.5) is 1.9m/s. Although this profile looks like a typical logarithmic profile, its adherence to the law of the wall is better visualized by plotting the non-dimensional velocity shear

$$\phi_m = \frac{\kappa z}{u_*}\frac{\partial \langle U \rangle}{\partial z}, \tag{13}$$

which is derived by integrating the law of the wall (Equation 9) from the roughness height to height z. This quantity should equal unity if the law of the wall is recovered, which is what we desire in the surface layer (the roughly lower 10%) of the tidal channel boundary layer. Fig. 3 shows a plot of ϕ_m, and there is clearly an overshoot in the profile below z/d = 0.04. This is a common problem in wall-modelled LES, sometimes called the "log-layer mismatch," in which the wall model and the actual LES are trying to match [19]–[21]. It is an area that we are working to improve.

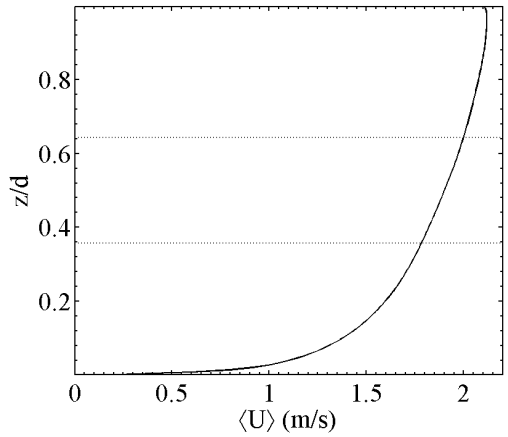

Fig. 2 Mean horizontal velocity profile of tidal channel precursor flow.

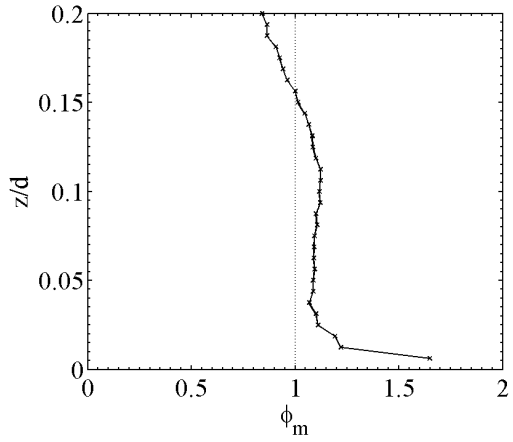

Fig. 3 Non-dimensional velocity shear profile of tidal channel precursor flow.

Resolved velocity variance profiles of the precursor flow are shown in Fig. 4. They follow the expected progression in which the streamwise velocity variance is greatest in magnitude, followed by the cross-stream, and finally the vertical. The streamwise velocity variance at the point nearest the wall should be greater than the values farther from the wall. There should not be a peak in streamwise velocity variance, as observed here, because wall-modeled LES does not resolve down to where the actual physically-occurring peak occurs. This problem is linked to the log-layer mismatch problem, and remedies are discussed in [21]–[22].

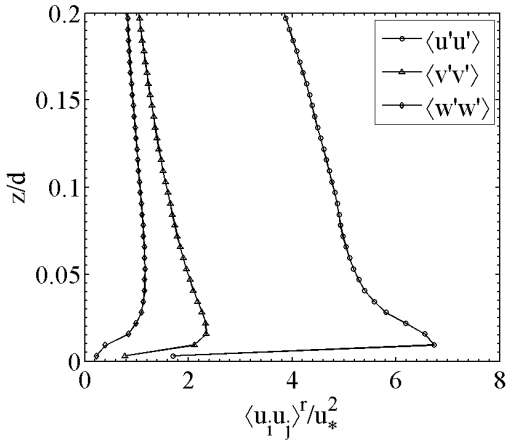

Fig. 4 Normalized velocity variances of the tidal channel precursor flow.

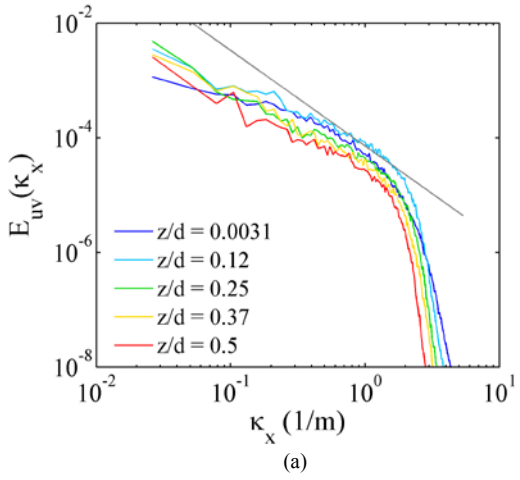

(a)

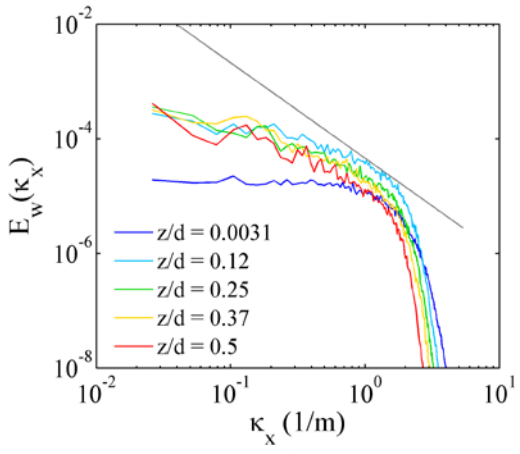

(b)

Fig. 5 One-dimensional spectra taken in the streamwise direction of (a) horizontal velocity and (b) vertical velocity at various heights.

Velocity spectra are also useful in assessing how well the precursor flow has been simulated. One-dimensional spectra of horizontal and vertical velocity taken in the streamwise direction at various heights are shown in Fig. 5. The horizontal velocity spectra exhibits a cascade region of -5/3 slope (gray line) followed by the LES filter cut-off at a wave

number of roughly 2, which is as expected. The vertical velocity contains a smaller -5/3 slope region. None of the spectra contain a peak, indicating that the domain size we chose is too small. The largest resolvable scales on this domain are the most energetic, but the domain should be able to resolve scales that are even larger, but less energetic.

The scales resolved can be visualized by examining contours of velocity on horizontal planes through the flow. Fig. 6 shows contours of instantaneous streamwise and vertical resolved velocity fluctuations on horizontal planes at two different heights. Both the streamwise and vertical velocity fluctuations are larger nearer the lower surface of the tidal channel, which agrees with the velocity variances being largest near the surface in Fig. 4. Elongated regions of lower- and higher-speed streamwise velocity are seen near the surface, and the domain is not long enough to accommodate an entire structure. At hub height, these elongated structures are not present, but large pockets of lower- and higher-speed regions exist. Here, the grid is not sufficiently wide to accommodate these pockets. The scale of the vertical velocity structures near the wall is much smaller than that of the streamwise velocity, and the domain seems large enough to accommodate them. This is reflected in the vertical velocity spectrum at the lowest level in Fig. 5(b). It shows that a peak would probably occur if the domain were enlarged slightly. At hub height, the vertical velocity structures are larger, but not as large as those of the streamwise velocity. Again, it appears that the domain should be larger to properly capture these large structures.

B. *Turbine Array Simulations*

An overview of a typical turbine array simulation flow field is shown in Fig. 7, which depicts an instance of the flow field from Case J. In red are positive isosurfaces of the second invariant of the velocity-gradient tensor, sometimes called the "Q criterion." This quantity is positive in regions of rotating flow, such as vortices. The tip and root vortices are seen spiraling behind the first two turbines. The vortex systems appear to break down about one diameter downstream. The turbulence created in the wake of the first row of turbines aids in breaking down the vortices of the second row of turbines, visible four diameters downstream of the first row. Note that the flow is periodic in the cross-stream direction, so only half of turbines T2 and T4 are seen in the second row. Streamwise velocity is volume rendered in Fig. 7, meaning that both color and opacity values are given to each "voxel" of the flow field. The opacity is set such that only the lower speed fluid, in the turbine wakes and near the tidal channel's lower surface, is visible in blue to light aqua. Note that the flow speeds in the wakes are significantly lower than the 1.9m/s inflow hub height average speed.

Fig. 8(a) shows contours of resolved streamwise velocity in a horizontal plane at hub height from Case B. The wake behind the first row of turbines is clearly visible with flow speeds reduced to roughly 1.2m/s. Note that since we are not modeling the nacelle, there is a region of higher speed fluid through the center of the rotor. To maintain continuity, the flow speed increases between the rotors. This suggests that a staggered configuration may be advantageous. The low speed wakes of the first row of turbines impinge upon the second row. The wakes of the second row of turbines exhibit streamwise velocities as low as 0.5 m/s. The second row of turbine wakes also appear to meander significantly and contain more turbulent motions.

Fig. 8(b) shows contours of resolved vertical velocity in the same horizontal plane as Fig. 8(a). Since the turbines in Case B all rotate clockwise as viewed from upstream, their wakes rotate counter-clockwise. This effect can only be captured using a turbine model that imposes tangential forces on the flow field, like the actuator line or an advanced actuator disk (see [23] for a discussion on the importance of including tangential forces in the turbine model).

To better understand wake evolution with downstream distance, it is useful to look at time-averaged velocity profiles. Fig. 9(a) shows the vertical profiles of time-averaged resolved streamwise velocity from the single turbine Case A taken at various downstream locations behind the turbine and aligned with the turbine's centerline. The wake is vertically asymmetric due to the vertical shear in the mean flow. As in Fig. 8, the velocity peak at the rotor's center is clearly observable. By about 5D downstream, where D is rotor diameter, this peak disappears, and the wake more closely resembles that of a bluff body. At 8D downstream, the velocity at the center of the wake is 22% lower than the ambient hub height average flow speed. In a tidal channel with more ambient turbulent intensity than the 6% simulated in this study, one would expect the wake recovery to be more aggressive than observed here. Fig. 9(b) shows horizontal profiles of time-averaged resolved streamwise velocity from Case A at various downstream locations and at hub height. The velocity profiles are asymmetric in this plane, as well. Notice that up to 5D downstream, there still exist two velocity minima adjacent to the wake centerline. The minima on the left side has a smaller velocity than that on the right. If you imagine the vertical profiles, shown in Fig. 9(a), rotated counter-clockwise, as viewed from upstream (the direction that this wake rotates), it is clear that the left minima should have a smaller velocity, since it corresponds to the part of the wake that was rotated from the lower momentum part of the wake nearest the tidal channel lower surface. The profile also is asymmetric at distances past the edge of the wake. The left side of the plot shows a higher than ambient velocity, while the right side shows one that is lower. This may have to do with the fact that our domain is not large enough to capture the largest turbulent structures. Fig. 6(b), which presents contours of instantaneous hub-height streamwise resolved velocity from the precursor, shows that the left side of the flow (as viewed from downstream looking upstream) contains a higher speed structure that is continuously cycled through the flow in the precursor. Likewise, there is a lower-speed structure on the right. When the precursor boundary data is saved, the effect of these structures is saved, and is applied to the turbine array domain. The effect shows up as a consistently higher-speed flow on the left side of Fig. 9(b) and a lower-speed flow on the right side.

Fig. 9(c) shows the time-averaged resolved streamwise velocity profiles taken in a horizontal plane at hub height from the staggered array Case I. Up to 3D downstream, the wakes of the two upstream turbines are clearly visible. At 4D and beyond, the wake of the downstream center turbine T3, and half the wakes of the downstream turbines T2 and T4 are visible. The inflow experienced by the downstream turbines in this case is above the ambient average hub height speed due to flow blockage caused by the upstream turbines. Because of this, the downstream turbines perform better than a single isolated turbine.

Table II outlines the time-averaged power produced, by each turbine and each case collectively, relative to the power produced by a single turbine (Case A). Values for turbines T2 and T4 from Cases I and J are not shown as they are unreliable because only half the turbine was computed. Turbine T0 in the front row always produces more power than the adjacent turbine T1. The same explanation applies here as that which explains why the left side of Fig. 6(b) has a time-averaged velocity in excess of ambient, whereas the right has one less than ambient. The high- and low- speed turbulent structures "trapped" on the left and right sides, respectively, of the precursor (as viewed from downstream looking upstream) causes turbine T0 to produce more power and T1 to produce less power.

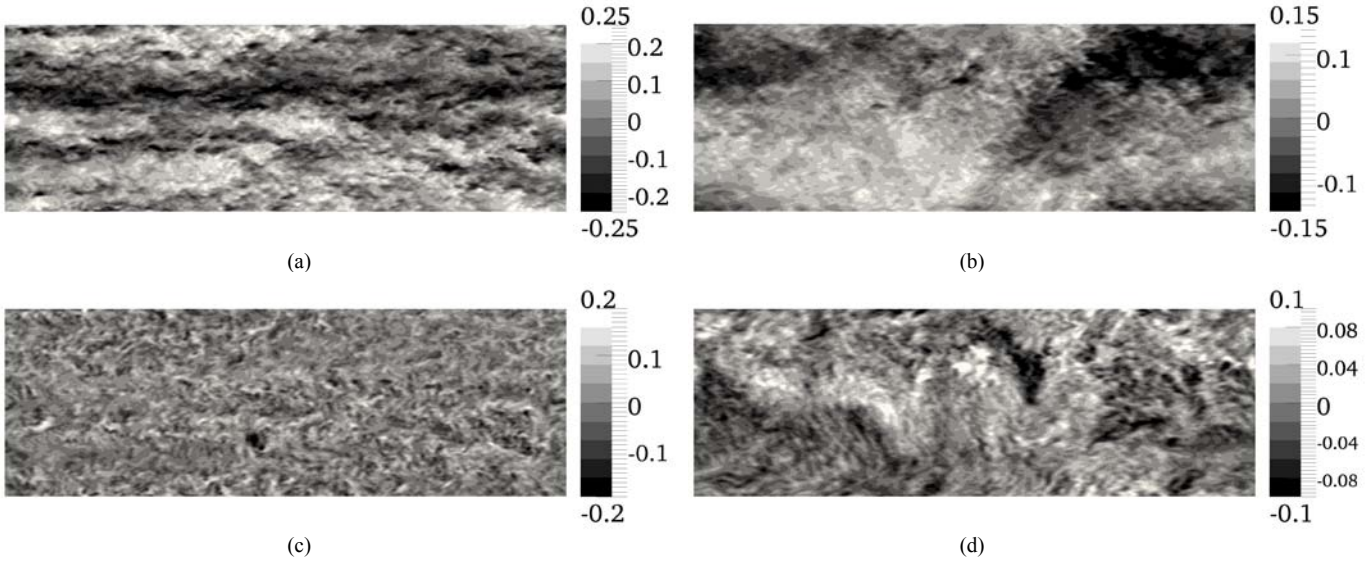

Fig. 6 Contours of instantaneous resolved velocity normalized by hub height velocity on horizontal planes. Contours (a) and (b) are of streamwise velocity, $\overline{u}/U_{hub}$, and (c) and (d) are of vertical velocity, $\overline{w}/U_{hub}$. Contours (a) and (c) are at $z/d = 0.1$, and contours (b) and (d) are at $z/d = 0.5$. Flow is from left to right.

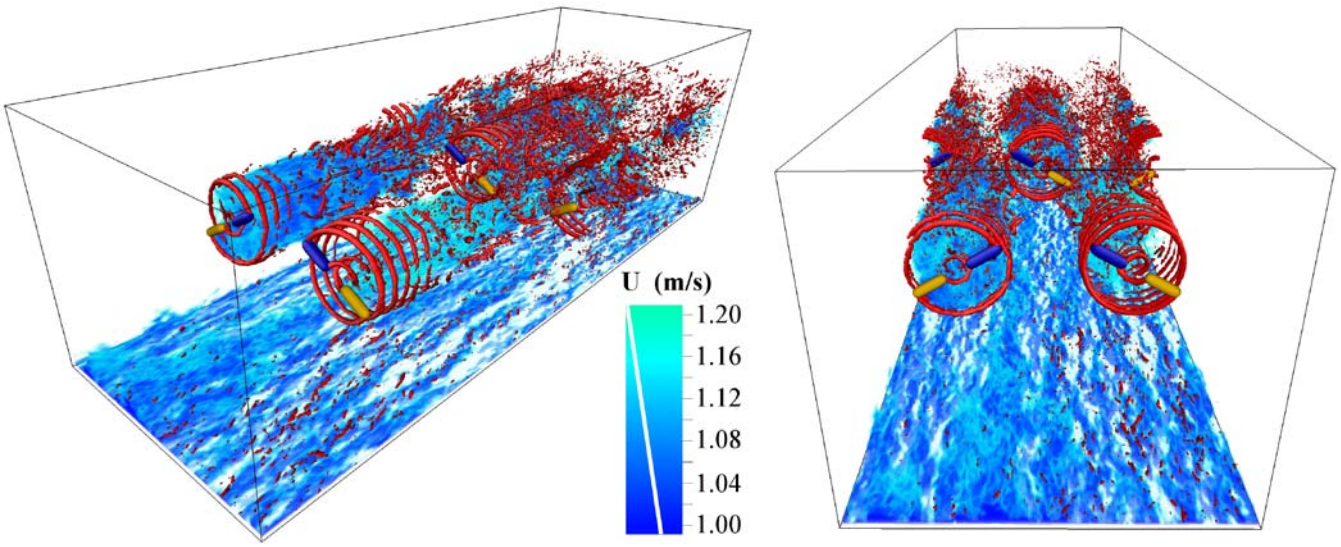

Fig. 7 Instantaneous views of the flow field from Case J with staggered counter-rotating turbines. Resolved streamwise velocity is volume rendered, and the colors correspond to different flow speeds, as shown in the color scale. The white line on the color scale indicates opacity of the volume rendering. The blue end of the scale is more opaque than the aqua end. The red isosurfaces are a positive value of the second invariant of the velocity-gradient tensor, denoting the locations of vortices. The purple and yellow isosurfaces are positive and negative values of the vertical component of the body force, respectively, created by the actuator lines. The view at left is from upwind and offset laterally. The view at right is from upwind. Cross-stream domain boundaries are periodic.

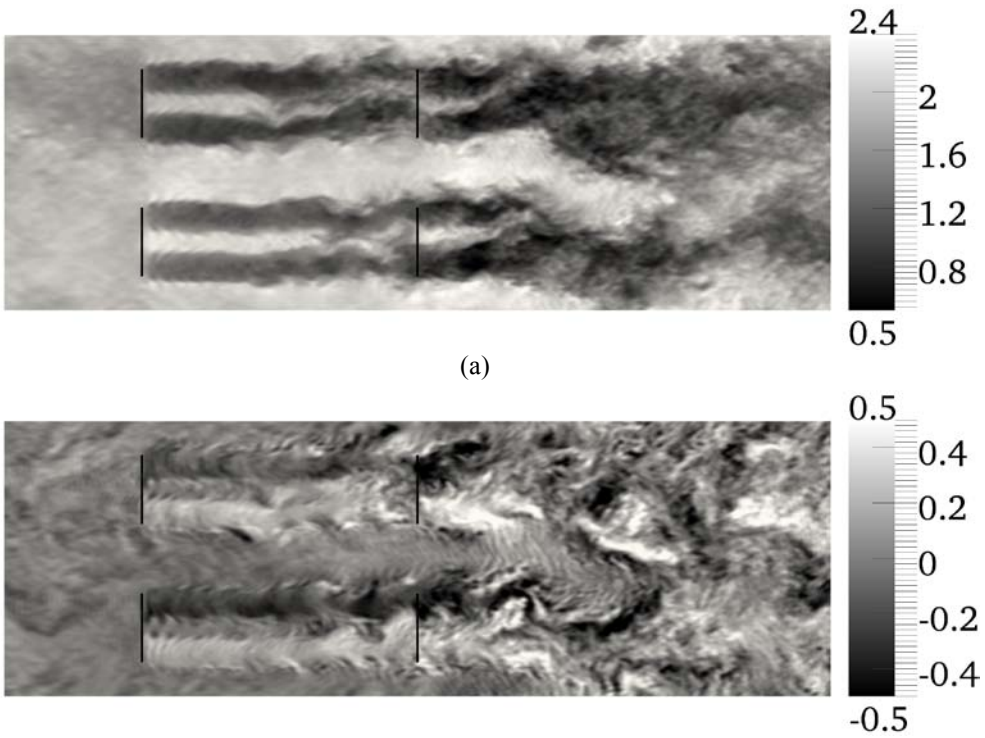

Fig. 8 Instantaneous contours of (a) resolved streamwise velocity and (b) resolve vertical velocity in a horizontal plane at the turbine hub height from Case B. The flow is from left to right, the black vertical lines denote the location of the rotor disks, and the units are m/s.

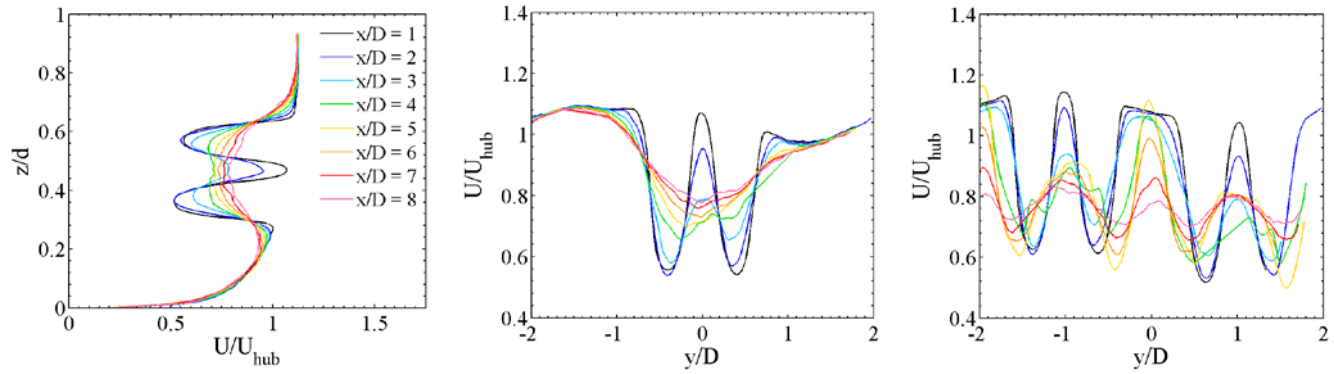

(a) (b) (c)

Fig. 9 Time-averaged resolved streamwise velocity profiles in the wakes of the tidal turbines. Vertical profiles aligned with the turbine centerline from Case A are shown in (a). Horizontal profiles at hub height from Case A and Case I are shown in (b) and (c), respectively.

It is also clear that for the non-staggered co-rotating Cases B-D, increases in the spacing between rows increase the overall array efficiency from 78% to 84%. However, staggering the downstream rows, even with a downstream spacing equivalent to the non-staggered Case B, produces the greatest benefit. The staggered Cases I and J perform more efficiently collectively than does the single turbine case A.

Counter-rotating the turbines has little effect on power produced. If consecutive turbines in a cross-stream row rotate counter to one another, but turbines downstream of one another co-rotate, there is no advantage (compare Case B to E). If however, the downstream turbines rotate counter to the next upstream turbines, an efficiency increase of about 3% is observed (compare Case B to F). Decreasing the cross-stream spacing of counter-rotating turbines in a row seems to have little effect (compare Case B to G and H).

V. Conclusions

Our initial work in applying LES to arrays of tidal turbines demonstrates that this methodology can provide useful unsteady information about wakes and power production. The accuracy of simulations performed within the framework

TABLE II
AVERAGE POWER OUTPUT FOR EACH CASE

	Average Relative Power $\langle P \rangle / \langle P_A \rangle$					
Case	**T0**	**T1**	**T2**	**T3**	**T4**	**Total**
A	1.000	–	–	–	–	1.000
B	1.155	0.925	0.593	0.478	–	0.788
C	1.156	0.926	0.642	0.531	–	0.814
D	1.156	0.926	0.697	0.584	–	0.841
E	1.156	0.925	0.593	0.477	–	0.788
F	1.156	0.925	0.600	0.481	–	0.791
G	1.130	0.943	0.577	0.498	–	0.787
H	1.134	0.966	0.554	0.484	–	0.785
I	1.155	0.924	–	1.045	–	1.041
J	1.156	0.924	–	1.036	–	1.038

presented here will be assessed as experimental field data become available. Although LES is more computationally-expensive than CFD based on the RANS equations, it yields a detailed, time-dependent solution that contains all of the large eddies within the flow. Such simulations could be used to develop improved RANS turbulence models for tidal turbine array calculations.

This work highlights that the application of tangential forces by the turbine model is important in recreating the wake asymmetry that exists behind actual turbines. However, there is currently a lack of wake data behind HATTs; a deficiency we plan to correct in the future.

This work also shows that the way in which the turbulent inflow is simulated greatly affects the wake propagation and power production of the array flow. For example, the domain we used here is not long enough to capture the largest scale structures that form in this flow. Therefore, a low speed structure as long as our domain became "trapped" in the domain and continuously cycled through it during the precursor. This caused the turbines on that side of the domain to consistently produce less power than the turbines on the other side. In the future, we plan to determine the domain size necessary to resolve the largest scales. We also plan to find tidal channel observation data with which to compare our precursor data.

In future studies, we plan to include the physics of salinity and temperature stratification and analyze its effect on the inflow and array performance. It would be interesting to simulate the tidal-cycle variation of the inflow, and its effect on the performance and efficiency of a tidal turbine array.

ACKNOWLEDGMENT

All computations were performed on the U.S. Department of Energy's Red Mesa computing system. Funding for this work was provided through the U.S. Department of Energy.

Michael Lawson provided useful discussion in performing these simulations along with specifications for the turbines modelled in this study. Tony Martinez provided the original development and implementation of our actuator line code. OpenCFD, the developers of the OpenFOAM software, are acknowledged for freely providing such a useful open-source tool to the community.

REFERENCES

[1] A. J. MacLeod, S. Barnes, K. G. Rados, and I. G. Bryden, "Wake effects in tidal current turbine farms", in *Proceedings of the International Conference of Marine Renewable Energy*, Newcastle upon Tyne, UK, 2002.

[2] S. Gant and T. Stallard, "Modelling a tidal turbine in unsteady flow," in *Proceedings of the Eighteenth (2008) International Offshore and Polar Engineering Conference*, Vancouver, BC, Canada, July 2008, pp. 473–480.

[3] X. Sun, J. P. Chick, and I. G. Bryden, "Laboratory-Scale Simulation of Energy Extraction from Tidal Currents," *Renewable Energy*, vol. 33, pp. 1267–1274, 2008. DOI: 10.1016/j.renene.2007.06.018.

[4] M. Li, S. Radhakrishnan, U. Piomelli, and W. Rockwell Geyer, "Large-eddy simulation of the tidal-cycle variation of an estuarine boundary layer", *Journal of Geophysical Research*, vol. 115, no. C08003, 2010. DOI: 10.1029/2009JC005702.

[5] G. Zhao, "Numerical simulation of complex channel flows," Ph. D. thesis, Department of Civil and Environmental Engineering, Stanford University, Stanford, CA, USA, May 2007.

[6] R. Booij, "Modelling the flow in curved tidal channels and rivers," in *Proceedings of the International Conference on Estuaries and Coasts*, Hangzhou, China, 2003, pp. 786–794.

[7] J. Smagorinsky, "General circulation experiments with the primitive equations," *Monthly Weather Review*, vol. 91, pp. 99–164, 1963.

[8] M. C. Richmond, J. Thomson, V. Durgesh, and B. Polagye, "Inflow characterization for marine hydrokinetic energy devices—FY-2010 annual progress report," Pacific Northwest National Laboratory, Richland, WA, PNNL Tech. Rep. PNNL-19859, 2011.

[9] C.-H. Moeng, "A large-eddy simulation model for the study of planetary boundary layer turbulence," *Journal of the Atmospheric Sciences*, vol. 41, no. 13, pp. 2052–2062, July 1984.

[10] J. N. Sørensen and W. Z Shen, "Numerical modeling of wind turbine wakes," *Journal of Fluids Engineering*, vol. 124, pp. 393–399, June 2002. DOI: 10.1115/1.1471361.

[11] W. Z Shen, M. O. L. Hansen, and J. N. Sørensen, "Determination of the angle of attack on rotor blades," *Wind Energy*, vol. 12, pp. 91–98, 2009. DOI: 10.1002/we.277.

[12] M. J. Lawson, Y. Li, and D. C. Sale, "Development and verification of a computational fluid dynamics model of a horizontal-axis tidal current turbine," in *Proceedings of the 30th International Conference on Ocean, Offshore, and Arctic Engineering (OMAE 2011)*, Rotterdam, The Netherlands, June 2011.

[13] OpenFOAM is a registered trade mark of OpenCFD Limited, the producers of OpenFOAM software. Available: http://www.opencfd.co.uk.

[14] C. M. Rhie and W. L Chow, "Numerical study of the turbulent flow past an airfoil with trailing edge separation," *AIAA Journal*, vol. 21, no. 11, pp. 1525–1532, 1983.

[15] R. I. Issa, "Solution of the implicitly discretized fluid flow equations by operator-splitting," *Journal of Computational Physics*, vol. 62, pp. 40–65, 1985.

[16] C.-H. Moeng and P. P. Sullivan, "A comparison of shear- and buoyancy-driven planetary boundary layer flows," *Journal of the Atmospheric Sciences*, vol. 51, no. 7, pp. 999–1022, April 1994.

[17] J. G. Brasseur and T. Wei, "Designing large-eddy simulation of the turbulent boundary layer to capture law-of-the-wall scaling," *Physics of Fluids*, vol. 22, no. 2, 2010. DOI: 10.1063/1.3319073.

[18] P. R. Spalart, M. K. Strelets, and A. Travin, "Expectations in the wall region of a large-eddy simulation", in *Quality and Reliability of Large-Eddy Simulations ERCOFTAC Series*," vol. 12, part III, pp. 189–191, 2008, DOI:10.1007/978-1-4020-8578-9_15.

[19] P. P. Sullivan, J. C. McWilliams, and C.-H. Moeng, "A sub-grid scale model for large-eddy simulation of planetary boundary layer flows," *Boundary-Layer Meteorology*, vol. 71, pp. 247–276, 1994.

[20] T. Wei and J. G. Brasseur, "The surface stress boundary condition in large eddy simulations of high Reynolds number turbulent boundary layer flows," to be submitted to *Boundary Layer Meteorology*, 2011.

[21] F. Porté-Agel, Y.-T. Wu, H. Lu, and R. J. Conzemius, "Large-eddy simulation of atmospheric boundary layer flow through wind turbines and wind farms," *Journal of Wind Engineering and Industrial Aerodynamics*, vol. 99, no. 4, pp. 154–168, 2011.